Dipolar interactions in Fe: A study with the neutron Larmor precession technique MIEZE in a longitudinal field configuration

S. Säubert,[1,2,*] J. Kindervater,[1,3] F. Haslbeck,[1,4] C. Franz,[1,2] M. Skoulatos,[1,2] and P. Böni[1,†]
[1]Physik-Department, Technische Universität München, D-85748 Garching, Germany
[2]Heinz Maier-Leibnitz Zentrum, Technische Universität München, D-85748 Garching, Germany
[3]Institute for Quantum Matter and Department of Physics and Astronomy, Johns Hopkins University, Baltimore, Maryland 21218, USA
[4]Institute for Advanced Studies, Technische Universität München, D-85748 Garching, Germany

(Received 7 March 2019; published 17 May 2019)

While the influence of dipolar interactions on the spin-wave dispersion in ferromagnets with localized magnetic moments has been studied in detail, similar studies in itinerant electron systems are rather scarce due to experimental difficulties. Using the newly developed neutron Larmor precession technique MIEZE in a longitudinal field configuration, we succeeded to map out the spin-wave dispersion in Fe at small momentum q and energy transfers E. The results demonstrate an excellent agreement of the magnon dispersion with the Holstein-Primakoff theory, which takes the dipolar interactions into account. At larger q, the data is in agreement with previous investigations by Collins *et al.*, Phys. Rev. **179**, 417 (1969). The q dependence of the linewidth of the magnons is proportional to $q^{2.5}$ in agreement with dynamical scaling theory. The critical exponent for the stiffness, $\mu = 0.35 \pm 0.01$, agrees with field theory. The spin dynamics in Fe is now explored by neutron scattering over an energy range $15\,\mu\text{eV} < E_{\text{sw}} < 120\,\text{meV}$, i.e., over about four orders of magnitude in energy.

DOI: 10.1103/PhysRevB.99.184423

I. INTRODUCTION

The detailed characterization of the magnetic excitations in magnetically ordered materials is of significant importance to improve their magnetic properties and to advance the understanding of their phase transitions. In light of the search for novel materials for applications—for example, skyrmionic [1] and multiferroic materials [2]—it is, in particular, the excitations at small momentum transfer q that are essential for the stabilization of new phases as they may stabilize textures with dimensions of a few nm up to a few μm. From the theoretical point of view, the universality of magnetic phase transitions with regard to the localization of the magnetic moments [3] and scaling theory [4] are of high interest.

With decreasing momentum transfer, interactions with energy scales that are much smaller than the exchange interactions become increasingly important and influence the magnetization dynamics. In most ferromagnets, it is the dipolar interaction that is the most important ingredient after the exchange interactions. It influences the magnetization dynamics [5] and their critical behavior [6,7], leading to the formation of magnetic domains and to depolarization effects on the spin dynamics. These effects are usually not considered in the interpretation of the spin-wave dispersions as measured by inelastic neutron scattering due to the lack of the required energy resolution.

In the model Heisenberg ferromagnet EuS, the observation of dipolar effects is most favorable due to the large magnetic moment $\mu_{\text{EuS}} = 7\,\mu_{\text{B}}$ and the small stiffness $D = 2.35\,\text{meV}\text{Å}^2$ at $0.72\,T_{\text{C}}$ [8]. Here, dipolar effects can be easily observed at momentum transfers of the order of $q \simeq 0.1\,\text{Å}^{-1} < q_{\text{D}} \simeq 0.25\,\text{Å}^{-1}$ [9,10]. The dipolar wave number q_{D} is related to the magnetization $M(T,H)$ and D by the expression [8]

$$D(T)q_{\text{D}}^2 = g\mu_0\mu_{\text{B}}M(T,H). \tag{1}$$

Here, g designates the gyromagnetic ratio, μ_0 the magnetic field constant, and μ_{B} Bohr's magneton. For EuS, the required resolution in energy and momentum can be easily achieved using triple-axis spectroscopy (TAS) with cold neutrons [11].

In contrast to EuS, itinerant ferromagnets such as the technologically important iron are rather challenging for the investigation of dipolar effects. Although the magnetic moment $\mu_{\text{Fe}} = 2.1\,\mu_{\text{B}}$ and therefore the magnetization, $M_{\text{s}}(295\,\text{K}) = 1.7 \times 10^6\,\text{A/m}$, are reasonably large; the large stiffness, $D(295\,\text{K}) = 281\,\text{meV}\text{Å}^2$ [12], yields according to Eq. (1) a small dipolar wave number $q_{\text{D}} = 0.045\,\text{Å}^{-1}$ [6,13]. Therefore, to identify dipolar effects, experiments have to be conducted at $q \ll q_{\text{D}}$ where the magnon energy is typically of the order of a few tens of μeV. Hence, in addition to the requirement of providing a tight q resolution, also an excellent E-resolution is necessary. These conditions cannot be easily realized by means of cold triple-axis spectrometers due to the strong penalty in intensity.

High-resolution measurements can, however, be realized by means of the MIEZE technique using a longitudinal field geometry [14]. It is based on a measurement of the Larmor precession of neutrons in a magnetic field. Because all spin manipulations of the neutrons are conducted before the sample position, the depolarization of the neutron beam by the

*steffen.saeubert@ph.tum.de; Present address: Department of Physics, Colorado State University, Fort Collins, Colorado 80523-1875, USA.
†peter.boeni@frm2.tum.de

Fe sample does not disturb the measurements, in contrast to conventional spin-echo techniques, where additional polarizers have to be installed to allow measurements in depolarizing environments [15].

To determine the influence of the dipolar interactions on the spin dynamics in the ordered phase of Fe, we have measured the intermediate scattering function,

$$I(q,\tau) = S(q,\tau)/S(q,0), \tag{2}$$

at and below T_C. The measurements extend the data of Collins *et al.* [12] and Lynn [16] to small q and the data of Kindervater *et al.* [17] from the paramagnetic phase to the ferromagnetic phase. The data are in excellent agreement with the theory of Holstein and Primakoff [18]. Finally, the q dependence of the linewidth of the spin waves Γ_{sw} is shown to be proportional to $q^{2.5}$ in agreement with the predictions of dynamical scaling theory [19].

II. EXPERIMENTAL SETUP

The neutron-scattering experiments were conducted at the beamline RESEDA [20] at the Heinz Maier-Leibnitz Zentrum using the MIEZE option in the longitudinal field configuration (LMIEZE) [14]. The setup was almost identical with the geometrical configuration that was used by Kindervater *et al.* for the study of the critical fluctuations in Fe [17]. Details of the setup and on the evaluation of the data are given in Appendix A.

The neutron beam with a wavelength $\lambda = 6$ Å and a wavelength band $\Delta\lambda/\lambda = 0.12$ was provided by a velocity selector. The two radio frequency spin flippers were operated at frequencies ν_1 and ν_2 up to a few hundred kHz with frequency differences in the range $1\,\text{Hz} \leqslant (\nu_2 - \nu_1) \leqslant 600\,\text{kHz}$, thus covering a dynamic range of approximately $6 \times 10^{-6}\,\text{ns} < \tau < 2\,\text{ns}$. To minimize path length differences and to achieve a high momentum resolution, the measurements were conducted in the small-angle neutron-scattering (SANS) configuration [20].

The scattered neutrons were recorded with a CASCADE detector [21], covering an area of 200 mm × 200 mm. To account for the instrumental resolution, all data was divided by the resolution function that was obtained by a measurement of the elastic scattering from a graphite sample. Note that in the SANS geometry, only spin fluctuations with transverse polarization contribute to the scattering cross section. To make a link to published measurements with TAS, a few scans were conducted at the beamline MIRA at FRM II [22].

We investigated a single crystal of bcc Fe that was used in previous studies [12,17,23]. It has a cylindrical shape with a diameter of 9 mm and a length of 25 mm. Its $\langle 111\rangle$ axis is oriented approximately 10° off the cylinder axis. The sample was mounted vertically in the neutron beam. A circular aperture with a diameter of 7 mm defined the illuminated sample volume. Most measurements were performed at temperatures $T_C - 21\,\text{K} \leqslant T \leqslant T_C$ ($T_C = 1043\,\text{K}$). A few scans have been conducted at room temperature. The sample was heated using a high-temperature furnace, with a resistive niobium double cylinder heating element.

The Curie temperature T_C of the sample was determined at the beginning of the experiment by measuring the temperature dependence of (i) the transmission of the neutrons through the sample and (ii) the small angle scattering caused by the critical magnetic fluctuations. The details of the measurements are described by Kindervater *et al.* [17]. The experiments yield $\tilde{T}_C = 1045.15 \pm 0.05\,\text{K}$ and a temperature gradient $\triangle T = \pm 0.1\,\text{K}$. In the following, we renormalize $\tilde{T}_C$ to the literature value $T_C = 1043\,\text{K}$. The reproducibility of T_C was periodically checked during the experiments by measuring the critical scattering during sweeping up and down the temperature through T_C.

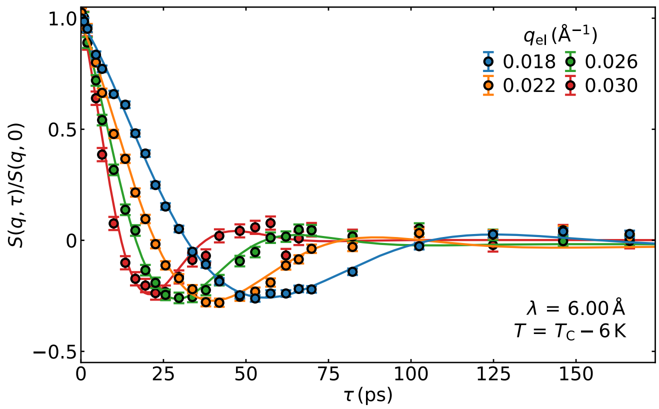

FIG. 1. q dependence of the normalized LMIEZE contrast in Fe as measured in the ferromagnetic phase at $T = T_C - 6\,\text{K}$. q_{el} designates the momentum transfer for zero energy transfer. The solid lines are fits to the intermediate scattering function Eq. (4) as explained in the text.

III. EXPERIMENTAL RESULTS

As explained in Appendix A, the use of an area detector allows measuring the intermediate scattering function $I(q,\tau)$ simultaneously over a wide range of momentum transfers q. Figure 1 shows some selected scans for momentum transfers $0.018\,\text{Å}^{-1} \leqslant q_{el} \leqslant 0.030\,\text{Å}^{-1}$. Here, q_{el} corresponds to the momentum transfer at zero energy transfer. As expected for damped magnons, $I(q,\tau)$ exhibits a damped oscillation. The period of the oscillations decreases with increasing q, reflecting the increase of the spin-wave energy with increasing q_{el} as expected. The decrease of the amplitude of the modulations with increasing τ indicates the damping of the excitations.

Figure 2(a) shows the temperature dependence of $I(q,\tau)$ for temperatures $T_C - 21\,\text{K} \leqslant T \leqslant T_C$ as measured for the momentum transfer $q_{el} = 0.18\,\text{Å}^{-1}$. The data shows that the period of the oscillation increases with increasing T, i.e., the magnons soften and evolve toward a quasielastic peak at $T = T_C$. We note that the data points at $T = T_C$ do not follow an exponential decay, i.e., the data points near $\tau = 25$ ps and $\tau = 80$ ps lie systematically above and below the exponential curve, respectively, confirming that the critical fluctuations at T_C do not decay exponentially [24,25].

To connect the LMIEZE data as measured in the time domain with spectroscopic data, we have calculated the Fourier transform of $S(q,\tau)$, yielding the scattering function [26]

$$S(q,\omega) = \frac{1}{2\pi\hbar}\int S(q,\tau)e^{-i\omega\tau}\,d\tau. \tag{3}$$

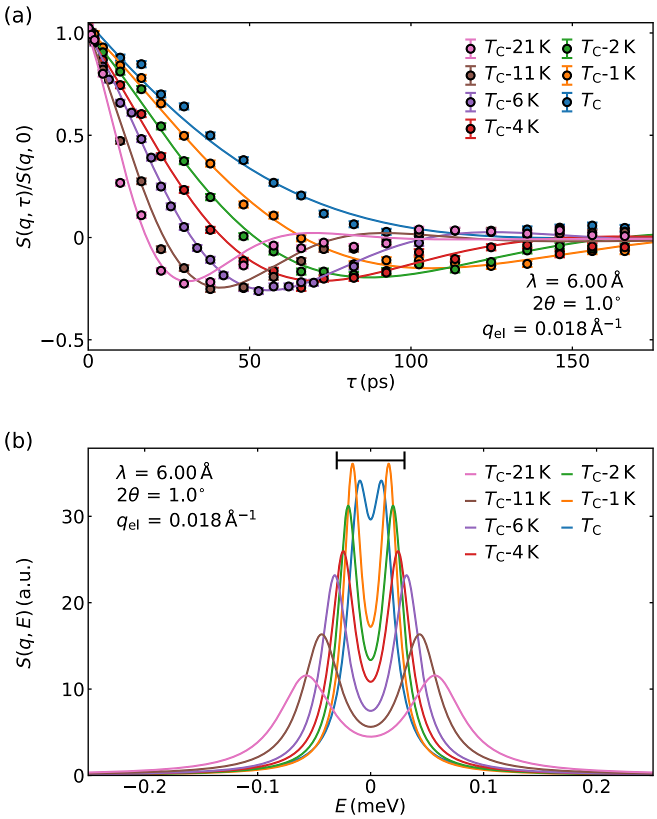

FIG. 2. LMIEZE measurements at T_C and in the ferromagnetic phase of iron at $q_{el} = 0.018\,\text{Å}^{-1}$. (a) Normalized intermediate scattering function $S(q,\tau)$, as measured using a MIEZE setup in a longitudinal field. Data was recorded using neutrons with a mean wavelength of $\lambda = 6.0$ Å. Note that the error bars are difficult to see because they are typically smaller than the size of the symbols. The solid lines are fits to the data using Eq. (4). (b) The scattering function $S(q,E)$ is shown for $q_{el} = 0.018\,\text{Å}^{-1}$ for various temperatures. The black horizontal line indicates the best energy resolution used by Collins *et al.* close to T_C [12].

Figure 2(b) shows that the magnon peaks shift with increasing temperature toward $E = 0$. The small double peak observed at T_C (blue solid line) may be an indication for the nonexponential decay of the critical fluctuations, i.e., that the spectrum at T_C cannot be described by a Lorentzian spectral weight function [25].

To extract the energy and the linewidth of the magnons, we have assumed that the line shape of the spin waves and the critical scattering can be represented by Lorentzian spectral weight functions. We have made this choice because in most work on the critical dynamics of isotropic ferromagnets around T_C, the data was fitted by means of Lorentzian spectral weight functions, in particular in the work of Collins *et al.* [12] to which we frequently refer to. Therefore, the intermediate scattering function is given by an exponentially decaying cosine function of the form

$$I(q,\tau) = \cos\left(\frac{E_{sw}\tau}{\hbar}\right)e^{-\Gamma_{sw}\tau/\hbar}, \qquad (4)$$

where E_{sw} and Γ_{sw} are the energy and the linewidth of the spin waves, respectively, and $\hbar$ is Planck's constant divided by 2π. Above T_C, $E_{sw} = 0$ and $I(q,\tau)$ becomes an exponential function.

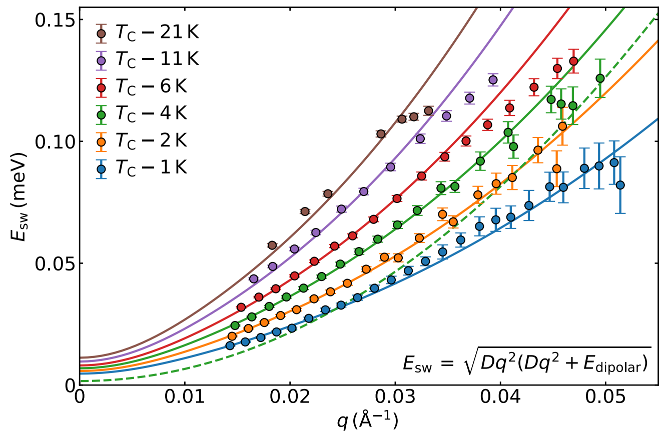

FIG. 3. Temperature dependence of the spin-wave dispersion. The solid lines are fits based on the Holstein-Primakoff theory [Eq. (7)] convoluted with the momentum resolution of RESEDA [Eq. (8)]. The dispersion becomes linear at small q. Note that the apparent gap at $q = 0$ is an artifact of the finite q-resolution. The broken green line depicts the dispersion when the dipolar interactions are neglected, i.e., $E_{sw} = Dq^2$. D is fixed at the value obtained for $T = T_C - 4$ K.

The spin-wave energy E_{sw} as a function of the scattering vector q is displayed in Fig. 3. While q_{el} used so far corresponds to the momentum transfer for zero energy transfer, q describes the momentum transfer at the peak position $E = E_{sw}$ of the spin wave. The data shows the expected increase of E_{sw} with decreasing temperature and increasing q. Appendix C provides a summary of the fitted parameters E_{sw} and Γ_{sw} for future theoretical analysis of the LMIEZE data.

Although the spin-wave spectrum is gapless, the resolution convoluted dispersions converge toward a finite energy for $q \to 0$ due to the finite q resolution. The systematic deviations of the data from the quadratic dispersion at large q appear because the measurements have been conducted in the proximity of the spectrometer configuration, where the scattering triangle does not close anymore. For a more detailed discussion of the magnon dispersion, see the next paragraph.

The q dependence of the damping, Γ_{sw}, of the spin waves is shown in Fig. 4(a) on a log-log scale. It is seen that Γ_{sw} is well reproduced by

$$\Gamma_{sw} = Aq^{z-\eta}, \quad z = 2.5, \qquad (5)$$

as expected according to the predictions of dynamical scaling theory [19]. The critical-point correlation exponent [27] $\eta = 0.0340 \pm 0.0025$ [28] has been neglected. The damping of the spin waves depends only weakly on T [Fig. 4(b)], i.e., the relative width Γ_{sw}/E_{sw} of the excitations decreases with decreasing temperature, leading to an apparent sharpening of the magnon peaks as expected [29,30].

The measured linewidth at T_C is with $A = 143 \pm 25\,\text{meV}\text{Å}^{2.5}$ in quantitative agreement with previous work [17,31,32] and the theoretical value $A = 128.6\,\text{meV}\text{Å}^{2.5}$ predicted by Frey and Schwabl [33]. The q dependence of Γ_{sw} is compatible with the experiments of Farago and Mezei who

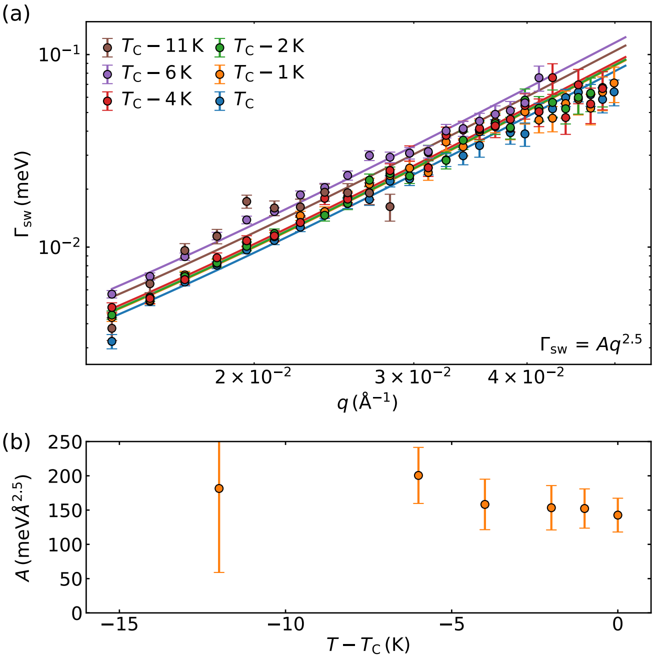

FIG. 4. (a) The momentum dependence of Γ_{sw} is shown for various temperatures at and below T_C. Γ_{sw} is roughly proportional to $q^{2.5}$. (b) Γ_{sw} depends only weakly on T in the temperature regime investigated.

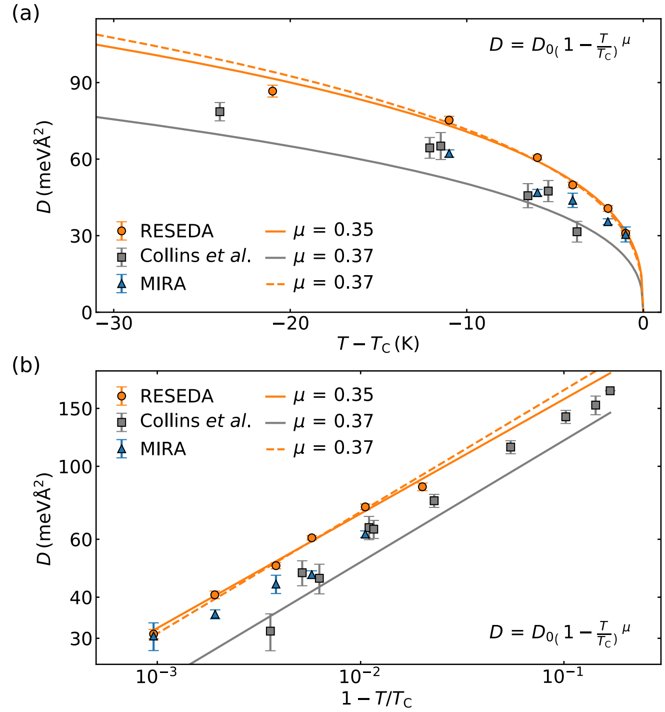

FIG. 5. Spin-wave stiffness D as function of temperature. The orange lines are fits to the LMIEZE-data using Eq. (9) with $\mu = 0.35$ (solid orange line) and $\mu = 0.37$ (broken orange line). The data of Collins *et al.* is shown by gray squares. Their fit to the data is shown as a gray line [12]. For comparison, the MIRA data are shown as blue triangles.

observed that $2 < z < 4$ [15]. An exponent $z = 2.5$ for the damping of the spin waves and the longitudinal fluctuations was also observed in Ni [34].

During the course of the LMIEZE experiment, we have not analyzed the polarization of the scattered neutrons. Therefore, the cross sections of the spin waves and the longitudinal fluctuations were measured simultaneously [11]. Hence, the magnitude of the damping of the spin waves is overestimated. However, the q dependence of Γ_{sw} is not affected.

IV. DISCUSSION

The spin-wave dispersions shown in Fig. 3 were analyzed using the theory of Holstein and Primakoff for isotropic ferromagnets including the dipolar interactions [18]:

$$E_{sw} = \big((E_q + g\mu_B\mu_0 H)(E_q + g\mu_B\mu_0 H + g\mu_B\mu_0 M(T,H)\sin^2\theta_{\boldsymbol{q}})\big)^{1/2}. \quad (6)$$

Here, $E_q = Dq^2$ designates the exchange energy, H the applied magnetic field, $\theta_{\boldsymbol{q}}$ the angle between the magnetization $\boldsymbol{M}$ and $\boldsymbol{q}$, and $g = 2$ is the Landé factor. Because no magnetic field was applied, $H = 0$ and $\langle(\sin\theta_{\boldsymbol{q}})^2\rangle = \frac{2}{3}$. Note that due to the very similar temperature dependence of D and M (see below), the theory of Holstein and Primakoff can also be applied at finite temperature and in particular close to T_C. Therefore, the dispersion simplifies to

$$E_{sw} = \big(Dq^2(Dq^2 + \tfrac{2}{3}g\mu_B\mu_0 M(T,H)\big)^{1/2}. \quad (7)$$

Note that $E_{sw} \propto q$ for $q \to 0$ [8] due to the reduction of the number of Goldstone modes from 2 to 1 by the dipolar interactions [5].

The spin-wave dispersions shown in Fig. 3 were fitted to Eq. (7) convolved with the instrumental momentum resolution $R(q - q', \sigma_{q-q'})$ of the spectrometer where $\sigma_{q-q'}$ is the spatial variance. R was analytically derived by Pedersen *et al.* [35] and Hammouda and Mildner [36] (see Appendix B). The fit function is then given by

$$E_{sw}(q - q_0) * R(q - q_0) = \int_{\mathbb{D}} E_{sw}(q - q_0) R(q' - (q - q_0), \sigma_{q'-(q-q_0)})\, dq'. \quad (8)$$

The apparent finite energy gap at $q = 0$ is an artifact of the finite q resolution, which leads to contributions of magnon scattering at finite q, where $E_{sw} > 0$. Therefore, there is no "dipolar" energy gap at $q = 0$. The agreement of our data with the Holstein-Primakoff theory is excellent.

To demonstrate the importance of including the dipolar interactions, we show in Fig. 3 the dispersion relation convolved with the resolution function for a purely exchange-coupled ferromagnet (green broken line), i.e., we have set $M(T,H) = 0$ in Eq. (7). Obviously, there is pronounced disagreement with the data. The apparent gap due to the momentum resolution around $q = 0$ is reduced because the dispersion now approaches $E = 0$ quadratically.

Figure 5 summarizes the temperature dependence of the spin-wave stiffness in Fe. The LMIEZE data of our paper (orange circles) is compared with the data obtained by Collins *et al.* (gray squares) [12] as well as with the data from MIRA (blue triangles). There is a good overall agreement between

TABLE I. Comparison of the spin-wave stiffness given by Collins *et al.* [12] to the results of the present paper. The calculated critical exponent μ is given by $\mu = 0.3407 \pm 0.0023$ [28].

	$\mu = \nu - \beta$	D_0 (meVÅ^2)
Collins *et al.* [12]	0.37 ± 0.03	281 ± 10
Säubert *et al.*	0.37 (fixed)	400 ± 23
(this paper)	0.35 ± 0.01	357 ± 20

the different data sets. The data from Collins *et al.* clearly deviate at small q from the LMIEZE and MIRA data in a systematic way, most likely because the use of thermal neutrons involved a coarse E resolution. Note that the MIRA data reproduces the data of Collins *et al.* at large q very well and maintain their trend toward small q.

It is also seen that the stiffness D as determined by TAS is larger than for LMIEZE because the two techniques sample different E regimes of the spectral weight function. TAS is more sensitive to large E transfers (corresponding to short times) and MIEZE is more sensitive to long times (corresponding to small E), respectively. As soon as the spectrum deviates from a Lorentzian, deviations will be observed.

The critical exponent for the temperature dependence of the stiffness D is given by $\mu = \nu' - \beta = \frac{1}{2}\nu'(1 - \eta)$, where ν' and β are the critical exponents for the correlation length below T_C and the magnetization, respectively [37]. Therefore, D is given by

$$D = D_0\left(\frac{T_C - T}{T_C}\right)^{\mu}, \tag{9}$$

where D_0 is a constant. In the following, we assume that the critical exponents for the correlation length below and above T_C are identical, i.e., $\nu' = \nu$. Therefore, one obtains, according to field theory, $\mu = 0.3407 \pm 0.0023$ [28], which is similar to the critical exponent of the magnetization, $\beta = 0.3647 \pm 0.0012$ [28].

Fitting the LMIEZE data to Eq. (9) yields $\mu = 0.35 \pm 0.01$ in excellent agreement with the theoretical value $\mu = 0.3407$. Collins *et al.* obtained $\mu = 0.37 \pm 0.03$, a value [12] that is compatible with our results within experimental error. We have also fitted $D(T)$ with the exponent μ fixed at 0.37 (broken orange line in Fig. 5), which does not agree as well with our data as the fitted value $\mu = 0.35$. The fit results of Collins *et al.* and our work are summarized in Table I.

V. CONCLUSIONS

Using the Larmor precession technique LMIEZE, we investigated the spin dynamics in the ferromagnetic phase of Fe close the the Curie temperature T_C with high resolution, thus extending the measurements of Collins *et al.* [12] and Lynn [16] to small q. Those measurements were performed with thermal neutrons, i.e., at momentum transfers where the dipolar interactions are small. As a result, the dispersion in Fe is now available over approximately four orders of magnitude in energy.

The results can be summarized as follows: The temperature dependence of the stiffness constant D is governed by the critical exponent $\mu = 0.35 \pm 0.01$ that is in excellent agreement with the theoretical value $\mu = 0.3407 \pm 0.0023$ [28]. The dipolar interactions do not affect μ; however, they reduce the number of Goldstone modes by one [5]. Therefore, the dispersion becomes linear in the limit $q \to 0$, i.e., the excitations are gapless. The damping of the spin waves displays a q dependence with a dynamic critical exponent $z = 2.5$ in agreement with scaling theory [4]. The comparison with similar measurements in localized systems shows that the qualitative behavior and the critical exponents in Fe are not affected by the localization of the magnetic moments.

The experiments in the ferromagnetic phase of Fe demonstrate that the LMIEZE technique is an excellent high-resolution spectroscopic technique for the investigation of the magnetization dynamics even under depolarizing conditions caused, for example, by domain formation or the application of magnetic fields. The very high energy resolution allows, in particular, the exploration of interactions with a small energy scale that may lead to emergent behavior in strongly correlated electron systems. Due to the very large dynamic range of the LMIEZE technique, it does not only complement the well-known triple-axis and time-of-flight techniques; in addition, it also extends these spectroscopies to very small energy and momentum transfers that are typically only accessible by conventional neutron spin-echo techniques.

In contrast to TAS that can be applied at small and large momentum transfers, the LMIEZE technique used in this study is essentially a time-of-flight-technique that provides the highest E resolution at small angles [38], where neutrons within a wide wavelength band $\Delta\lambda/\lambda \simeq 10\%$ can be used, leading to high intensity. For TAS, $\Delta\lambda/\lambda$ has to be restricted to $\simeq 1\%$, leading to a penalty of a factor of $\simeq$10 in intensity. For more details, see Ref. [39].

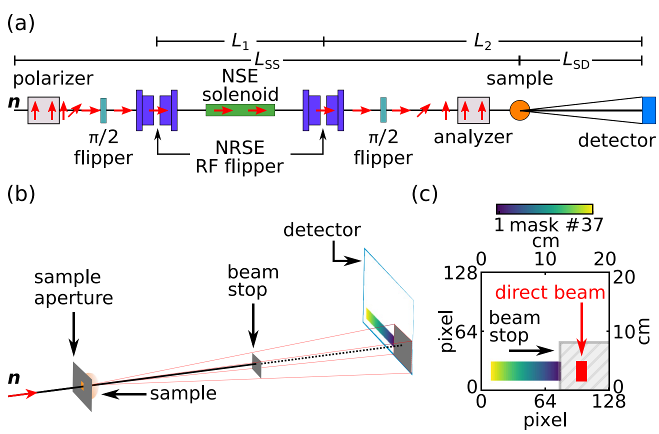

FIG. 6. (a) Sketch of the LMIEZE setup at the instrument RESEDA [17]. All spin manipulations are performed prior to the sample, thus making the method insensitive to depolarizing effects at the sample position. (b) Schematic of the neutron flight path showing sample, beam stop, and detector. (c) The black square indicates the detector area. The red rectangle shows the beam stop. Its shadow on the detector is visualized by the gray hatched area. The data was grouped in segments with a width of 2 pixels and a height of 20 pixels, centered along a line going through the direct beam (colored rectangle).

ACKNOWLEDGMENTS

We thank Robert Georgii, Christian Pfleiderer, Tobias Weber, and Andreas Wendl for very useful discussions. The work was supported through DFG TRR 80 (From Electronic Correlations to Functionality). The support by ERC AdG (No. 291079, TOPFIT) is gratefully acknowledged. The authors acknowledge the financial support by the Federal Ministry of Education and Research of Germany (BMBF) in the framework of Longitudinale Resonante Neutronen Spin-Echo Spektroskopie mit Extremer Energie-Auflösung (Project No. 05K16WO6). F.H., J.K., and S.S. acknowledge financial support through the TUM graduate school.

APPENDIX A: LONGITUDINAL MIEZE SETUP AT RESEDA (LMIEZE) AND DATA EVALUATION

The longitudinal MIEZE setup used for our experiments is shown in Fig. 6(a). Figure 6(b) shows a schematic of the neutron flight path. RESEDA utilizes a position sensitive 2D CASCADE detector which covers an area of 20×20 cm with 128×128 pixels. It provides the required high time resolution $\Delta = 100$ ns [21,40,41]. Figure 6(c) shows how the data from the detector was grouped for further processing. By comparing data evaluations using different grouping masks, it was shown that the integration of the counts over masks with a width of 2 pixels and a height of 20 pixels, i.e., approximately the height of the illuminated sample, allows processing data extending from $q_{\min} = 0.0139\,\text{Å}^{-1} \leqslant q \leqslant q_{\max} = 0.0629\,\text{Å}^{-1}$ while simultaneously retaining high statistics in the regions of interest.

TABLE II. Results obtained from fitting the spin-echo spectra at $T = T_C - 1$ K.

2θ (°)	q (Å^{-1})	E_{sw} (meV)	ΔE_{sw} (meV)	Γ_{sw} (meV)	$\Delta\Gamma_{sw}$ (meV)
0.96	0.0143	0.0162	0.0002	0.0095	0.0002
1.04	0.0157	0.0177	0.0002	0.0105	0.0002
1.12	0.0172	0.0195	0.0003	0.0124	0.0003
1.20	0.0187	0.0218	0.0003	0.0135	0.0004
1.27	0.0202	0.0233	0.0005	0.0157	0.0005
1.35	0.0218	0.0274	0.0005	0.0165	0.0006
1.43	0.0234	0.0309	0.0007	0.0198	0.0008
1.51	0.0249	0.0328	0.0008	0.0205	0.0009
1.59	0.0264	0.0359	0.0010	0.0235	0.0012
1.67	0.0280	0.0397	0.0013	0.0264	0.0015
1.75	0.0296	0.0431	0.0015	0.0287	0.0019
1.82	0.0312	0.0469	0.0018	0.0309	0.0022
1.90	0.0329	0.0508	0.0018	0.0296	0.0022
1.98	0.0345	0.0546	0.0029	0.0404	0.0035
2.06	0.0362	0.0595	0.0029	0.0384	0.0034
2.14	0.0380	0.0651	0.0039	0.0450	0.0045
2.22	0.0396	0.0678	0.0047	0.0499	0.0054
2.30	0.0410	0.0689	0.0046	0.0466	0.0053
2.38	0.0427	0.0737	0.0062	0.0557	0.0069
2.46	0.0447	0.0814	0.0060	0.0509	0.0065
2.54	0.0460	0.0811	0.0063	0.0519	0.0070
2.61	0.0480	0.0889	0.0083	0.0609	0.0090
2.69	0.0494	0.0899	0.0094	0.0639	0.0101
2.77	0.0508	0.0913	0.0089	0.0579	0.0095
2.85	0.0514	0.0821	0.0116	0.0690	0.0127

TABLE III. Results obtained from fitting the spin-echo spectra at $T = T_C - 2$ K.

2θ (°)	q (Å^{-1})	E_{sw} (meV)	ΔE_{sw} (meV)	Γ_{sw} (meV)	$\Delta\Gamma_{sw}$ (meV)
0.96	0.0145	0.0200	0.0002	0.0109	0.0002
1.04	0.0160	0.0232	0.0002	0.0120	0.0003
1.12	0.0176	0.0256	0.0003	0.0135	0.0003
1.20	0.0191	0.0285	0.0004	0.0147	0.0004
1.27	0.0206	0.0309	0.0005	0.0166	0.0005
1.35	0.0223	0.0354	0.0006	0.0182	0.0007
1.43	0.0238	0.0383	0.0007	0.0199	0.0008
1.51	0.0254	0.0418	0.0008	0.0211	0.0010
1.59	0.0272	0.0475	0.0010	0.0233	0.0012
1.67	0.0290	0.0525	0.0014	0.0287	0.0017
1.75	0.0303	0.0522	0.0017	0.0305	0.0020
1.82	0.0323	0.0603	0.0018	0.0299	0.0020
1.90	0.0345	0.0701	0.0026	0.0374	0.0028
1.98	0.0355	0.0670	0.0025	0.0347	0.0028
2.06	0.0379	0.0780	0.0035	0.0423	0.0037
2.14	0.0396	0.0826	0.0043	0.0471	0.0046
2.22	0.0411	0.0852	0.0049	0.0503	0.0054
2.30	0.0436	0.0964	0.0052	0.0483	0.0054
2.38	0.0459	0.1062	0.0078	0.0645	0.0082
2.46	0.0454	0.0888	0.0073	0.0591	0.0079

APPENDIX B: INSTRUMENTAL RESOLUTION OF THE LMIEZE SETUP

The resolution of the LMIEZE setup was analytically calculated following the theoretical work by Pedersen *et al.* [35] and Hammouda and Mildner: [36] (i) resolution due to the finite wavelength spread and (ii) resolution due to the finite collimation. The resolution function is represented by a Gaussian distribution of standard deviation σ_q, where q is the magnitude of the scattering vector,

$$R(q, \sigma_q) = \sqrt{\frac{1}{2\pi\sigma_q^2}} \exp\left(-\frac{q^2}{2\sigma_q^2}\right), \tag{B1}$$

with

$$\sigma_q^2 = \left(\sigma_q^2\right)_\lambda + \left(\sigma_q^2\right)_{\text{coll}}, \tag{B2}$$

$$= q^2\left(\frac{\sigma_\lambda}{\lambda}\right)^2 + \frac{4\pi^2}{\lambda^2}\frac{\sigma_x^2 + \sigma_y^2}{L_{\text{SS}}^2}, \tag{B3}$$

$$= q^2\left(\frac{\Delta\lambda}{\sqrt{6}\lambda}\right)^2 + \left(\frac{2\pi}{\lambda}\right)^2 \frac{\sigma_x^2 + \sigma_y^2}{L_{\text{SS}}^2}. \tag{B4}$$

In the last step, a triangular wavelength distribution was assumed. The spatial variance is divided in a horizontal

TABLE IV. Results obtained from fitting the spin-echo spectra at $T_C - 4$ K.

2θ (°)	q (Å^{-1})	E_{sw} (meV)	ΔE_{sw} (meV)	Γ_{sw} (meV)	$\Delta\Gamma_{sw}$ (meV)
0.96	0.0148	0.0244	0.0003	0.0131	0.0003
1.04	0.0164	0.0280	0.0003	0.0136	0.0003
1.12	0.0180	0.0323	0.0004	0.0150	0.0004
1.20	0.0197	0.0362	0.0005	0.0170	0.0005
1.27	0.0213	0.0398	0.0006	0.0190	0.0007
1.35	0.0230	0.0445	0.0007	0.0197	0.0008
1.43	0.0248	0.0496	0.0008	0.0216	0.0009
1.51	0.0266	0.0548	0.0011	0.0261	0.0013
1.59	0.0283	0.0599	0.0012	0.0260	0.0014
1.67	0.0302	0.0657	0.0015	0.0274	0.0016
1.75	0.0321	0.0716	0.0020	0.0332	0.0021
1.82	0.0343	0.0808	0.0026	0.0390	0.0028
1.90	0.0357	0.0815	0.0024	0.0340	0.0025
1.98	0.0381	0.0919	0.0038	0.0463	0.0040
2.06	0.0407	0.1037	0.0044	0.0488	0.0045
2.14	0.0412	0.0978	0.0048	0.0495	0.0050
2.22	0.0448	0.1172	0.0054	0.0509	0.0056
2.30	0.0458	0.1153	0.0062	0.0543	0.0065
2.38	0.0469	0.1146	0.0077	0.0626	0.0082
2.46	0.0495	0.1259	0.0079	0.0587	0.0083

contribution,

$$\sigma_x^2 = \left(\frac{L_{SD}}{L_{SS}}\right)^2 \frac{r_1^2}{4} + \left(\frac{L_{SS}+L_{SD}}{L_{SD}}\right)^2 \frac{r_2^2}{4} + \frac{1}{3}\left(\frac{\Delta x_3}{2}\right)^2, \quad \text{(B5)}$$

and a vertical contribution,

$$\sigma_y^2 = \left(\frac{L_{SD}}{L_{SS}}\right)^2 \frac{r_1^2}{4} + \left(\frac{L_{SS}+L_{SD}}{L_{SD}}\right)^2 \frac{r_2^2}{4} + \frac{1}{3}\left(\frac{\Delta y_3}{2}\right)^2. \quad \text{(B6)}$$

TABLE V. Results obtained from fitting the spin-echo spectra at $T = T_C - 6$ K.

2θ (°)	q (Å^{-1})	E_{sw} (meV)	ΔE_{sw} (meV)	Γ_{sw} (meV)	$\Delta\Gamma_{sw}$ (meV)
0.96	0.0154	0.0319	0.0003	0.0144	0.0003
1.04	0.0170	0.0361	0.0003	0.0157	0.0003
1.12	0.0186	0.0395	0.0004	0.0176	0.0004
1.20	0.0204	0.0448	0.0004	0.0201	0.0005
1.27	0.0223	0.0508	0.0005	0.0225	0.0006
1.35	0.0242	0.0570	0.0006	0.0240	0.0007
1.43	0.0259	0.0612	0.0008	0.0274	0.0009
1.51	0.0279	0.0680	0.0010	0.0291	0.0010
1.59	0.0302	0.0765	0.0012	0.0323	0.0013
1.67	0.0325	0.0858	0.0017	0.0386	0.0017
1.75	0.0347	0.0937	0.0018	0.0380	0.0018
1.82	0.0367	0.1001	0.0021	0.0395	0.0021
1.90	0.0388	0.1068	0.0023	0.0400	0.0023
1.98	0.0409	0.1137	0.0031	0.0488	0.0032
2.06	0.0432	0.1222	0.0035	0.0500	0.0037
2.14	0.0454	0.1299	0.0042	0.0538	0.0044
2.22	0.0470	0.1329	0.0049	0.0577	0.0052

TABLE VI. Results obtained from fitting the spin-echo spectra at $T_C - 11$ K.

2θ (°)	q (Å^{-1})	E_{sw} (meV)	ΔE_{sw} (meV)	Γ_{sw} (meV)	$\Delta\Gamma_{sw}$ (meV)
0.96	0.0165	0.0436	0.0004	0.0205	0.0005
1.04	0.0184	0.0487	0.0006	0.0232	0.0007
1.12	0.0204	0.0558	0.0007	0.0263	0.0008
1.20	0.0225	0.0626	0.0009	0.0281	0.0010
1.27	0.0249	0.0722	0.0013	0.0340	0.0013
1.35	0.0270	0.0794	0.0013	0.0327	0.0014
1.43	0.0296	0.0895	0.0015	0.0329	0.0016
1.51	0.0324	0.1011	0.0019	0.0360	0.0020
1.59	0.0349	0.1104	0.0022	0.0359	0.0022
1.67	0.0371	0.1177	0.0024	0.0358	0.0025
1.75	0.0393	0.1252	0.0025	0.0329	0.0026

The geometrical parameters of the LMIEZE setup are as follows:

Radius source aperture:	$r_1 = 20$	mm
Radius sample aperture:	$r_2 = 7$	mm
Source-sample distance:	$L_{SS} = 3.0$	m
Sample-detector distance:	$L_{SD} = 2.25$	m
Horizontal pixel width:	$\Delta x = 3.125$	mm
Vertical pixel width:	$\Delta y = 3.125$	mm
Wavelength:	$\lambda = 6.0$	Å
Wavelength spread:	$\Delta\lambda/\lambda = 0.12.$	

APPENDIX C: SUMMARY OF FIT PARAMETERS

Tables II–VII summarize the results obtained from fitting the spin-echo spectra recorded in the ferromagnetic phase of Fe between $T = T_C - 1$ K and $T = T_C - 21$ K. The data was fitted as described in the main text using Eq. (4). Some examples are shown for $T = T_C - 6$ K and various momentum transfers q in Fig. 1 and for fixed $q_{el} = 0.018$ Å^{-1} in Fig. 2.

TABLE VII. Results obtained from fitting the spin-echo spectra at $T_C - 21$ K.

2θ (°)	q (Å^{-1})	E_{sw} (meV)	ΔE_{sw} (meV)	Γ_{sw} (meV)	$\Delta\Gamma_{sw}$ (meV)
0.96	0.0183	0.0573	0.0007	0.0292	0.0008
1.04	0.0214	0.0712	0.0008	0.0302	0.0009
1.12	0.0236	0.0785	0.0010	0.0298	0.0010
1.20	0.0286	0.1030	0.0013	0.0319	0.0013
1.27	0.0306	0.1091	0.0012	0.0260	0.0012
1.35	0.0318	0.1101	0.0014	0.0255	0.0014
1.43	0.0332	0.1125	0.0019	0.0285	0.0018

[1] A. Fert, N. Reyren, and V. Cros, Nat. Rev. Mater. **2**, 17031 (2017).
[2] M. Fiebig, T. Lottermoser, D. Meier, and M. Trassin, Nat. Rev. Mater. **1**, 16046 (2016).
[3] T. Moriya, J. Magn. Magn. Mater. **100**, 261 (1991).
[4] P. C. Hohenberg and B. I. Halperin, Rev. Mod. Phys. **49**, 435 (1977).
[5] J. Kötzler, D. Görlitz, R. Dombrowski, and M. Pieper, Z. Phys. B **94**, 9 (1994).
[6] J. Kötzler, Phys. Rev. Lett. **51**, 833 (1983).
[7] J. Kötzler, J. Magn. Magn. Mater. **54-57**, 649 (1986).
[8] P. Böni, M. Hennion, and J. L. Martinez, Phys. Rev. B **52**, 10142 (1995).
[9] L. Passell, O. W. Dietrich, and J. Als-Nielsen, Phys. Rev. B **14**, 4897 (1976).
[10] H. G. Bohn, A. Kollmar, and W. Zinn, Phys. Rev. B **30**, 6504 (1984).
[11] P. Böni, B. Roessli, D. Görlitz, and J. Kötzler, Phys. Rev. B **65**, 144434 (2002).
[12] M. F. Collins, V. J. Minkiewicz, R. Nathans, L. Passell, and G. Shirane, Phys. Rev. **179**, 417 (1969).
[13] E. Frey, F. Schwabl, and S. Thoma, Phys. Rev. B **40**, 7199 (1989).
[14] M. Krautloher, J. Kindervater, T. Keller, and W. Häußler, Rev. Sci. Instrum. **87**, 125110 (2016).
[15] B. Farago and F. Mezei, Physica **136B**, 100 (1986).
[16] J. W. Lynn, Phys. Rev. B **11**, 2624 (1975).
[17] J. Kindervater, S. Säubert, and P. Böni, Phys. Rev. B **95**, 014429 (2017).
[18] T. Holstein and H. Primakoff, Phys. Rev. **58**, 1098 (1940).
[19] B. I. Halperin and P. C. Hohenberg, Phys. Rev. Lett. **19**, 700 (1967).
[20] C. Franz and T. Schröder, JLSRF **1**, 14 (2015).
[21] W. Häussler, P. Böni, M. Klein, C. J. Schmidt, U. Schmidt, F. Groitl, and J. Kindervater, Rev. Sci. Instrum. **82**, 045101 (2011).
[22] R. Georgii, T. Weber, G. Brandl, M. Skoulatos, M. Janoschek, S. Mühlbauer, C. Pfleiderer, and P. Böni, Nucl. Instrum. Methods Phys. Res. A **881**, 60 (2018).
[23] J. P. Wicksted, P. Böni, and G. Shirane, Phys. Rev. B **30**, 3655 (1984).
[24] P. Böni, M. E. Chen, and G. Shirane, Phys. Rev. B **35**, 8449 (1987).
[25] R. Folk and H. Iro, Phys. Rev. B **32**, 1880 (1985).
[26] G. L. Squires, *Introduction to the Theory of Thermal Neutron Scattering* (Dover Publications, N.Y., USA, 1996).
[27] K. G. Wilson and M. E. Fisher, Phys. Rev. Lett. **28**, 240 (1972).
[28] J. C. Le Guillou and J. Zinn-Justin, Phys. Rev. Lett. **39**, 95 (1977).
[29] V. G. Vaks, A. I. Larkin, and S. A. Pikin, Sov. Phys. JETP **26**, No. 3, 647 (1968).
[30] A. B. Harris, Phys. Rev. **175**, 674 (1968).
[31] G. Shirane, J. Magn. Magn. Mater. **45**, 33 (1984).
[32] F. Mezei, Phys. Rev. Lett. **49**, 1096 (1982).
[33] E. Frey and F. Schwabl, Phys. Lett. A **123**, 49 (1987).
[34] P. Böni, J. L. Martínez, and J. M. Tranquada, Phys. Rev. B **43**, 575 (1991).
[35] J. S. Pedersen, D. Posselt, and K. Mortensen, J. Appl. Cryst. **23**, 321 (1990).
[36] B. Hammouda and D. F. R. Mildner, J. Appl. Cryst. **40**, 250 (2007).
[37] O. W. Dietrich, J. Als-Nielsen, and L. Passell, Phys. Rev. B **14**, 4923 (1976).
[38] G. Brandl, R. Georgii, W. Häußler, S. Mühlbauer, and P. Böni, Nucl. Instrum. Methods Phys. Res. A **654**, 394 (2011).
[39] R. Georgii, J. Kindervater, C. Pfleiderer, and P. Böni, Nucl. Instrum. Methods Phys. Res. A **837**, 123 (2016).
[40] M. Klein and C. J. Schmidt, Nucl. Instr. Meth. Phys. Res. A **628**, 9 (2011).
[41] M. Köhli, F. Allmendinger, W. Häußler, T. Schröder, M. Klein, M. Meven, and U. Schmidt, Nucl. Instr. Meth. Phys. Res. A **828**, 242 (2016).